Synthesis and Optical Properties of Size-Quantized BiVO4 Semiconductor Particles with Tetragonal Zircon-Type Structure

Dragana Marinkovic *, Giancarlo Righini, Maurizio Ferrari

Posted Date: 26 March 2025

doi: 10.20944/preprints202503.1940.v1

Keywords: tetragonal nanostructured BiVO4; ethylene glycol-assisted synthesis; semiconductor; nanoparticles; optical properties; photocatalytic performance.

Article

Synthesis and Optical Properties of Size-Quantized $BiVO_4$ Semiconductor Particles with Tetragonal Zircon-Type Structure

Dragana Marinković [1,*], Giancarlo C. Righini [2] and Maurizio Ferrari [3]

[1] Vinča Institute of Nuclear Sciences, National Institute of the Republic of Serbia, University of Belgrade, P. O. Box 522, 11001 Belgrade, Serbia

[2] Nello Carrara Institute of Applied Physics (IFAC CNR), Sesto Fiorentino, Firenze, 50019, Italy

[3] Institute of Photonics and Nanotechnologies (IFN CNR, CSMFO Lab.) and FBK Photonics Unit, Via alla Cascata 56/C, Povo, Trento, 38123, Italy

* Correspondence: draganaj@vin.bg.ac.rs

Abstract: The optical characteristics of semiconductor's particles are strongly dependent on physicochemical properties and reduced size of the system. Decreasing the size of the material causes the increasing of the ratio between the number of atoms on the surface and the number of atoms inside the particle, that is, increasing of specific surface area and surface defects. Due to their high surface-area-to-volume ratio and increased number of active sites on the surface, the nanostructured materials with altered optical properties compared to the bulk material, are preferable for catalytic reactions. In this paper, ultra-small and very crystalline zircon-nanostructured bismuth vanadate ($BiVO_4$) semiconductor was prepared by ethylene glycol-assisted synthesis. The nanoparticles have radius between 2 and 8 nm, as shown by TEM images, and high Brunauer–Emmett–Teller (BET) specific surface area. The optical, structural, microstructural and photocatalytic properties were examined in detail. X-ray photoelectron spectroscopy (XPS) technique confirmed the occurrence of Bi, V, and O elements and also found that Bi and V exist in +3 and +5 oxidation states, respectively. The photocatalytic activity of the samples was checked using methyl orange (MO) under UV/Vis and Solar illumination. The photocatalytic performance was compared to commercial TiO_2 powder. The results showed tetragonal zircon-type nanostructured $BiVO_4$ as a promising catalyst for rapid removal of pollutants from wastewaters.

Keywords: tetragonal nanostructured $BiVO_4$; ethylene glycol-assisted synthesis; semiconductor; nanoparticles; optical properties; photocatalytic performance

1. Introduction

In recent decades, an immense research attention has been focused on the development of novel methods of fabrication of multifunctional nanostructured materials with unusual physical, electrical and optical properties originated from the strong quantum confinement effect or surface defects. The successful development of the multifunctional nanostructured materials opens a broad spectrum of new opportunities for their applications in sensor -basedchip devices, electromagnetic interference shielding, energy generation and storage, chemical- bio- and electro-sensing, fuel cells, multimodal imaging and photothermal therapy, solar and photovoltaic cells and photocatalytic water splitting [1–10].

The nanostructured materials with high surface area show improved chemical reactivity, magnetic moment and polarizability and enhanced photoactivities under UV/Vis light irradiation, in comparison to larger particles or bulk materials, due to increasing number of the photo-generated electron–hole pairs on the surface [11,12].

 doi:10.20944/preprints202503.1940.v1

Among all nanostructured materials, the bismuth-based compounds have been extensively studied in the last decade due to their broad spectrum of potential applications. Among all bismuth-based compounds, publications based on bismuth orthovanadate ($BiVO_4$) have seen an exponential increase in number over the last years. These compounds have many interesting and unique properties originating from the electronic and/or steric influences of the $6s^2$ lone pair of Bi^{3+} that has a strong role in determining the site occupancy of the Bi^{3+} ions. The bismuth-vanadate ($BiVO_4$) is widely applied as a yellow pigment [13], photoelectroanalytical sensor [14], ferroelectric material [15], antibacterial agent [16], luminescent material and a host for rare-earth ions [17,18], as well as a photocatalytic material [19].

$BiVO_4$ exists in nature in three crystalline forms: orthorhombic pucherite, tetragonal dreyerite (tz-$BiVO_4$, zircon-type structure, space group I41/amd), and monoclinic clinobisvanite (ms-$BiVO_4$, distorted scheelite-type structure, space group I2/b) [20]. Up to date, large number of methods has been adopted for the preparation of ms-$BiVO_4$, such as: hydrothermal method with and without using surfactant or template [21–23], microwave-assisted hydrothermal [24,25], solvothermal [26], and co-precipitation method [27]. Several methods have also been utilized for the synthesis of tz-$BiVO_4$: co-precipitation method [28–31], hydrothermal method [32–36], rapid microwave assisted method [37] and epitaxial growth on FTO substrate [38]. An enhanced photocatalytic activity of un-doped or no hybrid tetragonal zircon-type nanostructured $BiVO_4$ semiconductor is reported in dozen published papers [39]. Recently, MOF- derived tetragonal $BiVO_4$ and rare-earth doped $BiVO_4$ systems [40–43] with enhanced photocatalytic properties for water splitting were studied, where the presence of RE^{3+} could induce the progressive stabilization of the tetragonal phase [44].

This work was motivated by recent evidence that tetragonal zircon-type $BiVO_4$, tz-$BiVO_4$, one of three commonly found polymorphs of $BiVO_4$, is moderately photocatalytically active [45]. Only 30 or so relevant papers can be found in the literature: thus, tz-$BiVO_4$ has not been extensively studied and, in particular, its photocatalytic properties are insufficiently examined, new synthetic approaches to tz-$BiVO_4$ are most needed [46,47]. Interestingly, synthesis of tz-$BiVO_4$ in a non-aqueous medium is an obvious way to avoid hydrolysis and precipitation of side products.

Herein, aiming at producing nanocrystalline tz-$BiVO_4$ a new and non-conventional way of synthesis was attempted through a novel straightforward room-temperature non-aqueous preparation method. The as-prepared colloids and the obtained nanostructured particles were examined with a view of quantum size effects on their optical properties and their suitability in photocatalytic applications. The ultra-small tetragonal zircon-type $BiVO_4$ nanostructures, with size range from 2 to 8 nm, were prepared by ethylene glycol-assisted colloidal route and characterized using optical, structural and microscopic techniques. These size-quantized nanoparticles present a remarkable synthetic achievement. Adsorption behaviors and mechanisms of methyl orange on the size-quantized tetragonal $BiVO_4$ nanoparticles were studied in details, as well as photocatalytic activities. Good optical performances and enhanced photocatalytic activity in comparison to titania photocatalyst Degussa P25, give to the size-quantized tetragonal $BiVO_4$ nanoparticles the potential for different applications such as degradation of methyl orange (MO) and other organic dye-pollutants.

2. Materials and Methods

2.1. Materials and Chemicals Used

All chemicals were of high purity and were used without further purification. These included: bismuth(III) nitrate pentahydrate ($Bi(NO_3)_3x5H_2O$, Sigma-Aldrich, 97%), ammonium metavanadate (NH_4VO_3, Alfa Aesar, 99.999%), trisodium citrate dihydrate ($Na_3C_6H_5O_7x2H_2O$, ≥99%, Sigma–Aldrich), ethylene glycol ($C_2H_6O_2$, Sigma-Aldrich, 97%), polyethylene glycol 200 (PEG-200, Alfa Aesar), nitric acid, HNO_3 (J.T. Baker, 65%) distilled water, methyl orange ($C_{14}H_{14}N_3NaO_3S$, Merck) and titanium(IV) oxide nanopowder, Degussa P25 (Sigma-Aldrich, > 99.0%).

 doi:10.20944/preprints202503.1940.v1

2.2. Synthesis of Colloidal Tetragonal $BiVO_4$

Colloidal $BiVO_4$ samples were synthesized by modified ethylene glycol-assisted colloidal route at room temperature [48]. Here, NH_4VO_3 and $Bi(NO_3)_3x5H_2O$ were used as precursors and ethylene glycol was utilized as a solvent for precursors, in order to avoid the hydrolysis of $Bi(NO_3)_3$ and precipitation of side products like bismuth(III)-hydroxonitrate, a reaction medium for a precipitation and a capping agent (to limit a particle growth and prohibit agglomeration). Ethylene glycol is a dihydroxy alcohol ($HO–CH_2–CH_2–OH$) that is liquid at room temperature; it is more viscous than water, biodegradable and boils at 197 °C. There are also additional advantages of an ethylene glycol-mediated synthesis; this is one of the most general and powerful methods for preparation of high-quality nanomaterials, is used for conventional glassware and the synthesis is simple, easily scalable, "green", versatile and low-cost [49]. PEG-200 has role as a structure-directing agent to synthesize vanadate nanoparticles, as an organic additive and as a surface modifier.

The appropriate amounts of NH_4VO_3, $Bi(NO_3)_3x5H_2O$ were separately dissolved in ethylene glycol to prepare different concentrations of bismuth and vanadium solutions precursors (0.075M, 0.050M and 0.025M). The same concentration of solution of trisodium citrate together with HNO_3 was added dropwise to a solution at a stoichiometric ratio of Bi^{3+} ions at room temperature. A white precipitate consisting of a Bi^{3+}-Cit^{3-} complex was formed. The PEG-200 in ethylene glycol solution (with the same concetrations as precursors) was slowly, drop wise, added into the NH_4VO_3 containing solution and the resulting mixture was left under vigorous stirring for 1 hour. Afterwards, the ethylene glycol mixture solution of precursor of Bi^{3+} was slowly added into the mixture solution of NH_4VO_3 and PEG-200 under vigorous stirring for 2 hours and orange-yellow transparent colloids of $BiVO_4$ were obtained. It is important to emphasize that this preparation procedure proved to be fully reproducible over multiple trials, and, in all the as-prepared colloids, no evidence of precipitation has been noticed over a period of more than one year, thus indicating superior colloid stability of $BiVO_4$ nanoparticles in ethylene glycol solution. These colloids, corresponding to concentrations of precursor 0.075M, 0.050M and 0.025M, are hereafter referred to as samples A, B, C, respectively. In order to obtain the powders of $BiVO_4$, following the synthesis of colloidal $BiVO_4$, as-prepared colloids were additionally treated, centrifugated, washed with water several times and dried in an oven at 110°C for 24h. In the following, powders prepared using the colloids (A, B and C) are denoted as A-tz, B-tz and C-tz.

2.3. Characterization Methods and Instrumentation

Absorption measurements were performed by the UV-vis spectrophotometer (LLG-uniSPEC 2 UV/VIS-Spectrometer 190-1100 nm) in a range of wavelengths from 300 to 500 nm with 1 nm step. X-ray photoelectron spectroscopy (XPS) data were collected using a PHI Versa Probe III-XPS-spectrometer equipped with a monochromatic Al-Kα X-ray source and a hemispherical analyzer. Phase and purity of the powder samples were examined by powder X-ray diffraction (XRD) measurements on a Rigaku SmartLab diffractometer using Cu-Kα radiation (λ = 0.15405 nm). Diffraction data were collected with a step size of 0.02° and a counting time of 0.7°/min over the angular range 2θ from 15° to 70°. The photoluminescence (PL) measurements were recorded at room temperature on a Fluorolog-3 spectro-fluorimeter in the range of wavelengths from 450 nm to 600 nm. HRTEM measurements were performed using a FEI Tecnai F20 at 200 kV electron acceleration voltages after drop-casting of sample material on lacey carbon TEM grids.

2.4. Photocatalytic Experiment

Methyl orange (MO), anionic and water soluble azo dye, was widely used material in the dye industry and is commonly selected as a model organic pollutant to evaluate the behavior of a material for the removal of organic pollutants from its aqueous solutions. The removal of MO in aqueous solutions was carried out in double-walls cylindrical photochemical reactor. Temperature was maintained at 18° C by continuous flow of water through the reactor walls during the adsorption and

 doi:10.20944/preprints202503.1940.v1

photocatalytic experiments. Adsorption experiments were carried out in the dark before subsequent (photodegradation) experiments with visible light illumination. The suspension of $BiVO_4$ powder and solution of MO was than exposed to visible light from a LED lamp (Xled E27-15W, 220 V, 3000 K, 1350Lm) placed 15 cm above the reactor.

In a typical experiment, MO was dissolved in 200 ml of deionized water to obtain a 5 mgL^{-1} solution while optimal photocatalyst concentration was found to be 1 $mgmL^{-1}$. Prior to irradiation, the adsorption−desorption equilibrium of the dye on the photocatalysts surface was achieved through the vigorous stirring for 90 minutes in the dark to ensure adsorption/desorption equilibrium before lighting. During the irradiation procedure, the reaction sample was collected and centrifuged to remove photocatalyst particles. The change in dye concentration over time was monitored by measuring the absorbance of MO at wavelength of 464 nm using the UV-Vis spectrophotometer. At given time intervals, samples were collected from the reaction mixture during 240 minutes of irradiation.

3. Results and Discussion

3.1. Optical Properties of Colloidal $BiVO_4$ Nanoparticles

3.1.1. UV-Vis Absorption and Photoluminescent Spectra

It is a well-known fact that the optical properties of semiconducting nanoparticles are essentially determined by their energy band gap (Eg). $BiVO_4$ is a semiconductor with a direct optical band gap with energy of 2.9 eV for tetragonal structure, measured at room temperature [50]. The optical UV-Vis absorption spectra of dispersions of colloidal tz-$BiVO_4$ nanoparticles in ethylene-glycol are given in Figure 1a. It is noteworthy that there are very few reports in the literature on absorption spectra of solutions of any polymorph of $BiVO_4$ [51–53]; UV-Vis diffuse reflection spectra, however, are more common [28,54,55]. It was observed that all the prepared samples exhibited absorption bands in the near UV and in the blue-violet regions. The absorption, centered at around 362 nm can be readily explained by ligand-to-metal charge transfer transitions localized within tetrahedral vanadate VO_4^{3-} groups; electrons from filled oxygen 2p levels are excited into vacant vanadium 3d levels [56,57].

The extended absorption tail in UV-Vis spectrum is assigned to subgap absorption due to defect states or intra-band absorption [57].

In general, the band gap energies of semiconducting materials can be extracted from their absorption spectra by using Tauc's plots, i.e., by plotting $(\alpha h\nu)^{1/n}$ versus incident photon energy hν. The determination of optical band gap is obtained by Tauc's Equation (1):

$$(\alpha h\nu)^{1/n} = A(h\nu - E_g), \quad (1)$$

where A is a proportionality constant, α is the measured optical absorption coefficient and Eg is the band gap energy of the material. The exponent n depends on the type of the transition and the values of n = 1/2, 2, and 3/2, are for direct allowed transitions, indirect allowed and direct forbidden transitions, respectively. To determine the type of transitions, $(\alpha h\nu)^{1/n}$ versus hν was plotted; the band tail constant A is obtained through the slope of the linear region of the graphs, while the corresponding optical band gaps were estimated by extrapolating to zero absorption in the linear part of the graph at $(\alpha h\nu)^{1/n} = 0$ Tauc's plots (with n = 1/2) of the three as-prepared samples of colloidal $BiVO_4$ are given in Figure 1b. The estimated band-gap values of 3.07, 3.09 and 3.12 eV are higher than the value of 2.9 eV reported for tz-$BiVO_4$ [31]. The calculated values of band gaps are shifted to larger values than those for bulk materials due to quantum confinement. Obtained Eg values are in agreement with reported band gap values by other authors for tz-$BiVO_4$ nanoparticles. [57,58]

 doi:10.20944/preprints202503.1940.v1

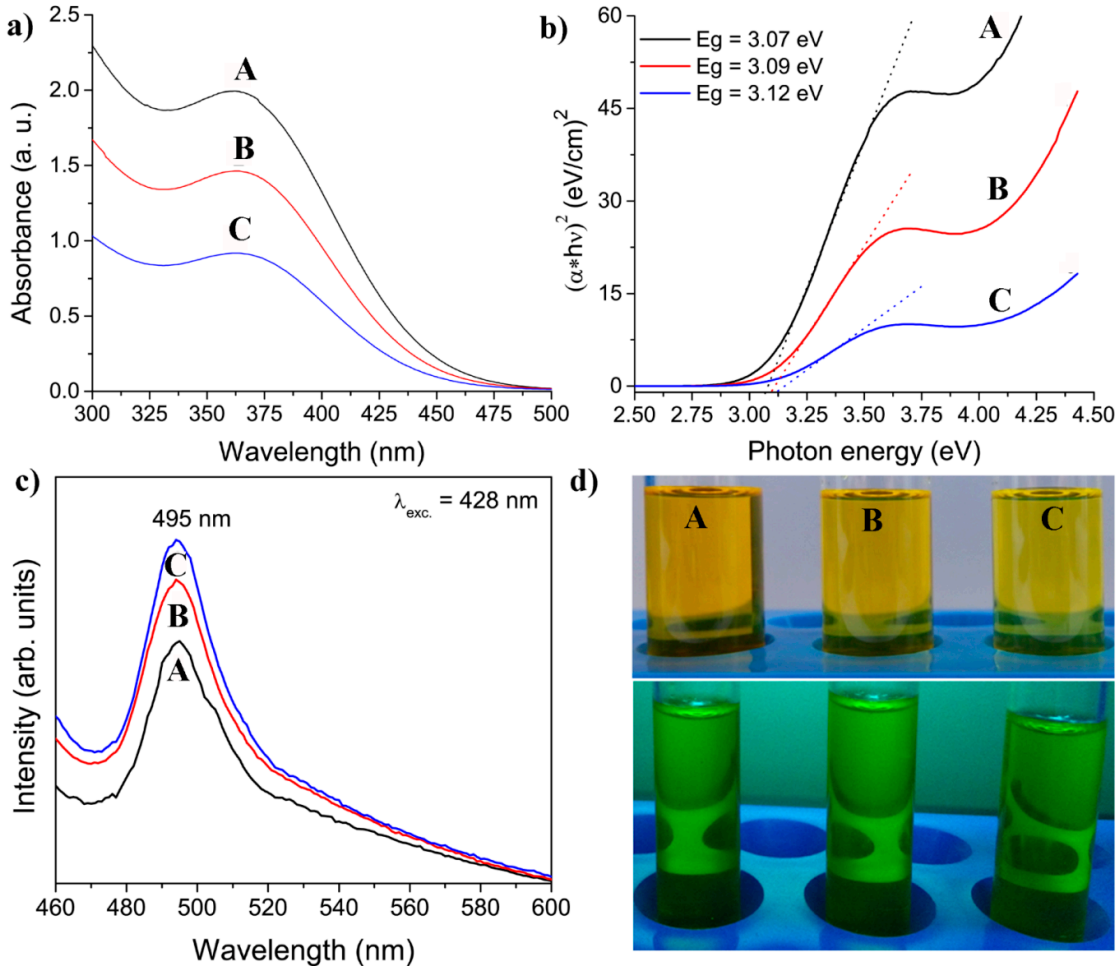

Figure 1. Optical properties of colloidal dispersions of tz-$BiVO_4$ nanoparticles in ethylene glycol; a) UV-Vis absorption spectra; b) Tauc`s plots and band-gap energy estimates; c) Photoluminescent emission spectra; d) Photographs of colloids under day light (top) and a UV-lamp (bottom).

The radius (r) of the nanoparticles were estimated using Brus equation [59]:

$$E_{g(nano)} = E_{0(bulk)} + \left(\frac{1}{m_e^*} + \frac{1}{m_h^*}\right)\frac{h^2}{8m_0r^2} - \frac{1.8e^2}{4\pi\varepsilon\varepsilon_0 r} \quad , \qquad (2)$$

where $E_{g(nano)}$ is the values of the energy gap determined as the x-intercept of the linear portion of the absorbance as a function of wavelength for nanoparticles with unknown radius (r); $E_{0(bulk)}$ is the energy gap for bulk material ($E_{0(bulk)}$ = 2.90 eV, for tetragonal $BiVO_4$) [60], me* and mh* are the effective masses of electrons and holes (m_{e^*} = 17.322×m_e, m_{h^*} = 1.210 × m_e) for tetragonal $BiVO_4$, respectively [61], m_0 is the mass of electron (m_0 = 9.110x10^{-31} kg), ε_0 is the permittivity of vacuum (ε_0 = 8.854187817×10^{-12} F×m^{-1}), ε is the dielectric constant for the tetragonal-$BiVO_4$ (ε = 68) [62], h is the Planck constant (h = 6.62607004×10-34 m^2kgs^{-1}) and e is the charge of an electron (e = 1.60217662×10^{-19} C). The second term in equation (2), which dominates when r is small, corresponds to the confinement energies for an electron–hole pair in a spherical nanoparticles, while the third term accounts for the Coulomb interaction between an electron and hole modified by the screening of charges by the crystal. After multiplying by r^2, rearranging, and using the quadratic formula:

$$r = \frac{-\left(\frac{1.8e^2}{4\pi\varepsilon\varepsilon_0}\right) + \sqrt{\left(\frac{1.8e^2}{4\pi\varepsilon\varepsilon_0}\right)^2 + \left(E_{g(nano)} - E_{g(bulk)}\right)\frac{h^2}{2m_0}\left(\frac{1}{m_e^*} + \frac{1}{m_h^*}\right)}}{2\left(E_{g(nano)} - E_{g(bulk)}\right)}, \qquad (3)$$

 doi:10.20944/preprints202503.1940.v1

one obtains the radii (r) of the nanoparticles equal to 3.24, 3.20 and 3.12 nm, for A, B, and C samples, respectively. These values are consistent with average nanoparticles size determined from TEM images.

Photoluminescent spectra, PL, with excitation wavelength at 428 nm of dispersions of tz-$BiVO_4$ nanoparticles are shown in Figure 1c. A vanadate group, VO_4^{3-}, where the central vanadium ion is coordinated by four oxygen ions in a tetrahedral (Td) symmetry, is known to be an efficient luminescent center. Hence, strong emission band centered at 495 nm could be attributed to the charge-transfer transitions (generated upon photo-excitation) between vanadium 3d and oxygen 2p orbitals in VO_4^{3-}. The results presented in this paper are similar to those of Bajaj et al. [28]. Photographs of colloidal solutions under day light and UV-lamp (253 nm) are presented in the Figure 1d.

3.1.2. XPS Spectra

To explore the chemical states of surface Bi and V sites in tetragonal nanostructured $BiVO_4$ semiconductor, the X-ray photoelectron spectroscopy (XPS) technique was used. Figure 2a presents the wide energy range 0-1200 eV XPS survey spectrum of $BiVO_4$ nanoparticles with tetragonal structure.

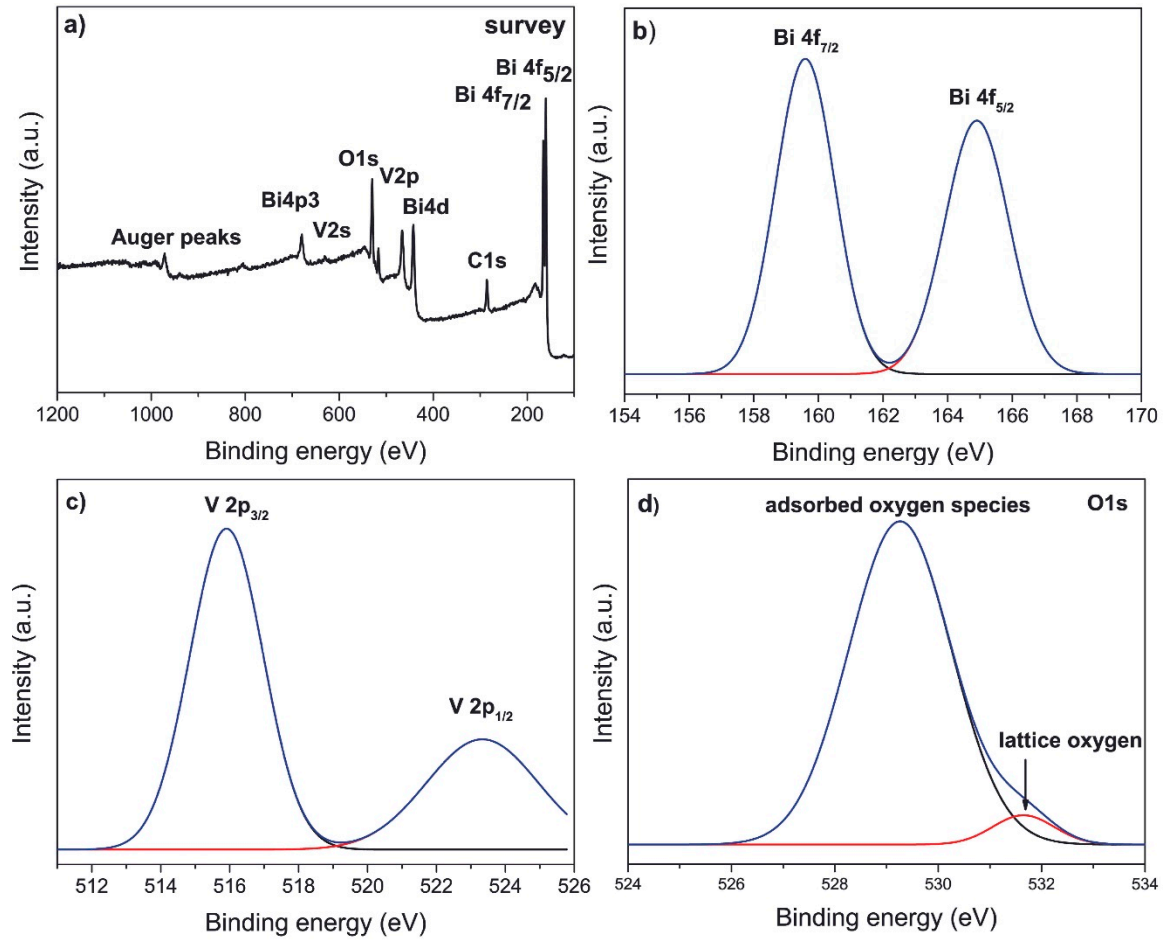

Figure 2. a) XPS survey spectrum with core level spectra of b) Bi 4f, c) V 2p and d) O 1s tetragonal nanostructured $BiVO_4$ semiconductor.

The binding energy levels of Bi, V and O, along with the Auger peaks, identified from the XPS survey spectrum, indicate that no other impurity elements or secondary phases were found in obtained $BiVO_4$ nanoparticles. The C1s peak arises from the reference. The chemical binding energy of C 1s at 284.54 eV was used for calibration to adjust the binding energies of the other elements. As

 doi:10.20944/preprints202503.1940.v1

it can be seen from Figure 2b, the Bi 4f orbital of tz-$BiVO_4$ can be well reproduced by two peaks with binding energies of 159.60 eV and 164.91 eV, which can be assigned to the Bi $4f_{7/2}$ and Bi $4f_{5/2}$ orbitals of Bi^{3+} indicating the absence of the metallic state of Bi^0.The Bi4f photoelectron core level spectra point out a spin orbit splitting of about 5.31 eV between Bi $4f_{7/2}$ and Bi $4f_{5/2}$ peaks and corresponds to the binding energy of the Bi^{3+} state. For the V2p region (Figure 2c), the peaks located at binding energies of 515.91 eV and 523.37 eV are assigned to V $2p_{3/2}$ and V $2p_{1/2}$ of V^{5+}, respectively. Figure 2d presents the high-resolution O1s spectra of the $BiVO_4$ photocatalyst, which were fitted into two components at binding energy values of 529.28 and 531.71 eV, which can be assigned to the lattice oxygen and oxygen of surface hydration of the nanostructured tz-$BiVO_4$ [63]. The obtained values for binding energies of Bi4f, V2p and O1s are in accordance with literature [64–66].

3.1.3. Photocatalytic Performance

The photocatalytic activities of the tz-$BiVO_4$ samples were evaluated for the photodegradation of MO, which was used as a model of organic pollutants. The powders A-tz, B-tz and C-tz were evaluated for photocatalytic performance, and compared with performance of powdered Degussa P25, a standard commercially available photocatalyst, by photocatalytic degradation of MO, under simulated solar light.

Upon reaching the equilibrium (under no illumination) the initial time was chosen and the dye solution with photocatalyst was exposed to simulated solar light for 240 minutes. As is customary, a relative concentration (C/C_0) of MO versus a contact time t describes kinetics of the dye removal, C_0 and C being respectively the concentration of MO before illumination (t = 0) and the concentration of MO after illumination for t min, while the decolorization efficiency is defined as percentage of decreasing absorbance intensity according to the following equation:

$$\% \text{ decolorization} = (A_0\text{-}A)/A_0*100\%, \quad (4)$$

where A_0 is the absorbance at the maximum absorption wavelength (464 nm) of initial methyl orange solution, and A is the maximum absorption wavelength at 464 nm of the same solution mixed with ultra-small tz-$BiVO_4$ nanoparticles after the treatment. The efficiency of commercial TiO_2 P25 in removing the MO dye was found to be about 10%, while efficiencies of about 26%, 32% and 29% were observed for the samples A-tz, B-tz and C-tz, respectively, as presented in Figure 3a. The proposed mechanisms of the photocatalytic oxidation of MO in presence of tz-$BiVO_4$ photocatalyst are drawn in Figure 3b. Although still preliminary, this is a remarkably good performance of the system for MO removal and it would be interesting to examine it further for use in environmental purification [67]. This result suggests that ultrasmall tetragonal zircon-type $BiVO_4$ nanoparticles have a good photocatalytic performance and could be used in water and wastewater treatments, due to their large surface area and good efficiency under UV/Vis and solar light. Before doing any of the experiments, stability of methyl orange was tested under the proposed photocatalytic conditions. MO showed great stability under the conditions (lamp, temperature, etc.) used for all photocatalytic experiments confirming that the decreasing absorbance intensity should be attributed exclusively to the presence of $BiVO_4$ nanoparticles. The absorbance band at 464 nm corresponds to the conjugated structure that was associated with the azo bond (–N=N–) under the strong influence of the electron-donating dimethylamino group. Decreasing of absorbance intensity at 464 nm for A-tz, B-tz and C-tz Degussa P25 is presented in Table 1.

Table 1. Absorbance intensity at 464 nm for A-tz, B-tz, C-tz and Degussa P25 at different times.

Time/minutes	A-*tz*	B-*tz*	C-*tz*	Degussa P25
0	0.399	0.394	0.38	0.369
10	0.306	0.301	0.342	0.380
30	0.295	0.274	0.32	0.345
60	0.285	0.265	0.306	0.362

 doi:10.20944/preprints202503.1940.v1

90	0.29	0.256	0.292	0.381
120	0.269	0.244	0.285	0.38
180	0.258	0.229	0.270	0.315
240	0.230	0.212	0.227	0.346

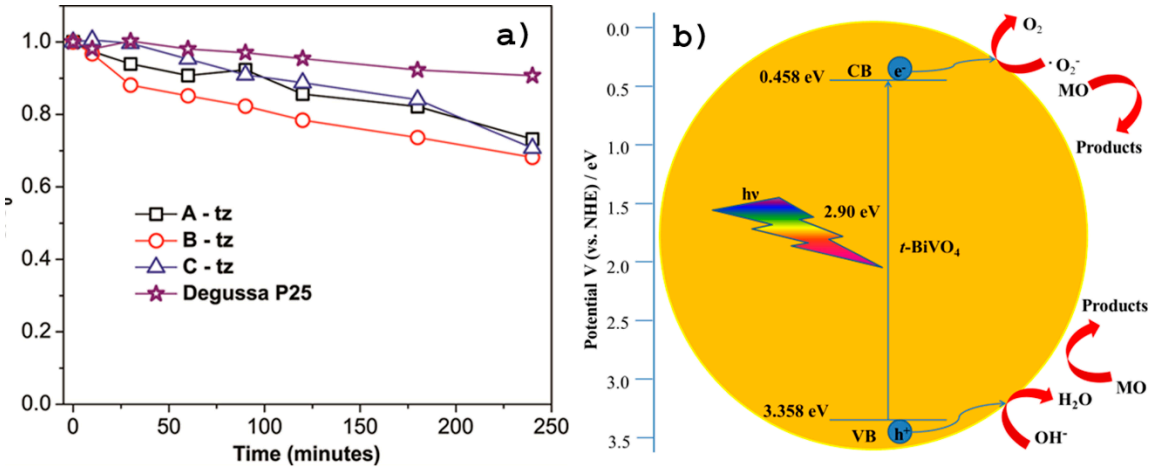

Figure 3. a) Photodegradation curves of MO solution (5 mg/L) by different tz-$BiVO_4$ samples and Degussa P25 (1 g/L) under simulated solar lighting and b) Proposed mechanisms of the photocatalytic oxidation of MO in presence of tz-$BiVO_4$ photocatalyst.

The possible mechanism of the photocatalytic oxidation of MO over tz-$BiVO_4$ can be represented by the following equations:

$$\text{tz-BiVO}_4 + h\nu \rightarrow \text{BiVO}_4\,(e^-) + \text{BiVO}_4\,(h^+)$$

$$\text{MO} + \text{hv} \rightarrow \text{MO}^*$$

$$\text{tz-BiVO}_4 + \text{MO}^* \rightarrow \text{BiVO}_4\,(e^-) + \cdot\text{MO}^+$$

$$\text{tz- BiVO}_4\,(e\text{-}) + \text{O}_2 \rightarrow \cdot\text{O}^{2-}$$

$$\cdot\text{MO}^+ + \text{O}_2/\cdot\text{O}^{2-} \rightarrow \text{intermediate product,} \qquad (5)$$

Under irradiation with visible-light tz-$BiVO_4$ nanoparticles can be excited to electron–hole pairs and the electron would transform the valence band to the conduction band of tz-$BiVO_4$. At the same time, the photo-generated electrons are transferred to the excited state (MO*) of the MO owing to the intramolecular π–π* transition. The photogenerated electrons of MO* are immediately injected into the CB of $BiVO_4$, leaving ·MO+ radicals [68,69].

3.2. Structural and Microstructural Properties

Representative high-resolution TEM (HRTEM) images of $BiVO_4$ particles of the as-synthesized colloidal dispersions A, B and C are depicted in Figure 4 (see Figures 4a, 4d and 4g). All TEM specimens were prepared by evaporating a drop of a colloidal dispersion of $BiVO_4$ in ethylene glycol on a carbon-coated specimen grid. Well-defined, non-agglomerated highly crystalline nanoparticles together with the diffractogram patterns produced from the digitally-recorded HRTEM images of the samples by means of the two-dimensional Fast Fourier Transformation (FFT) (see Figure 4b, 4e and 4h) can be seen in the TEM micrographs. The nanoparticle with size of 6-8 nm, 4-6 nm and 2-4 nm were found in the samples A, B and C, respectively.

 doi:10.20944/preprints202503.1940.v1

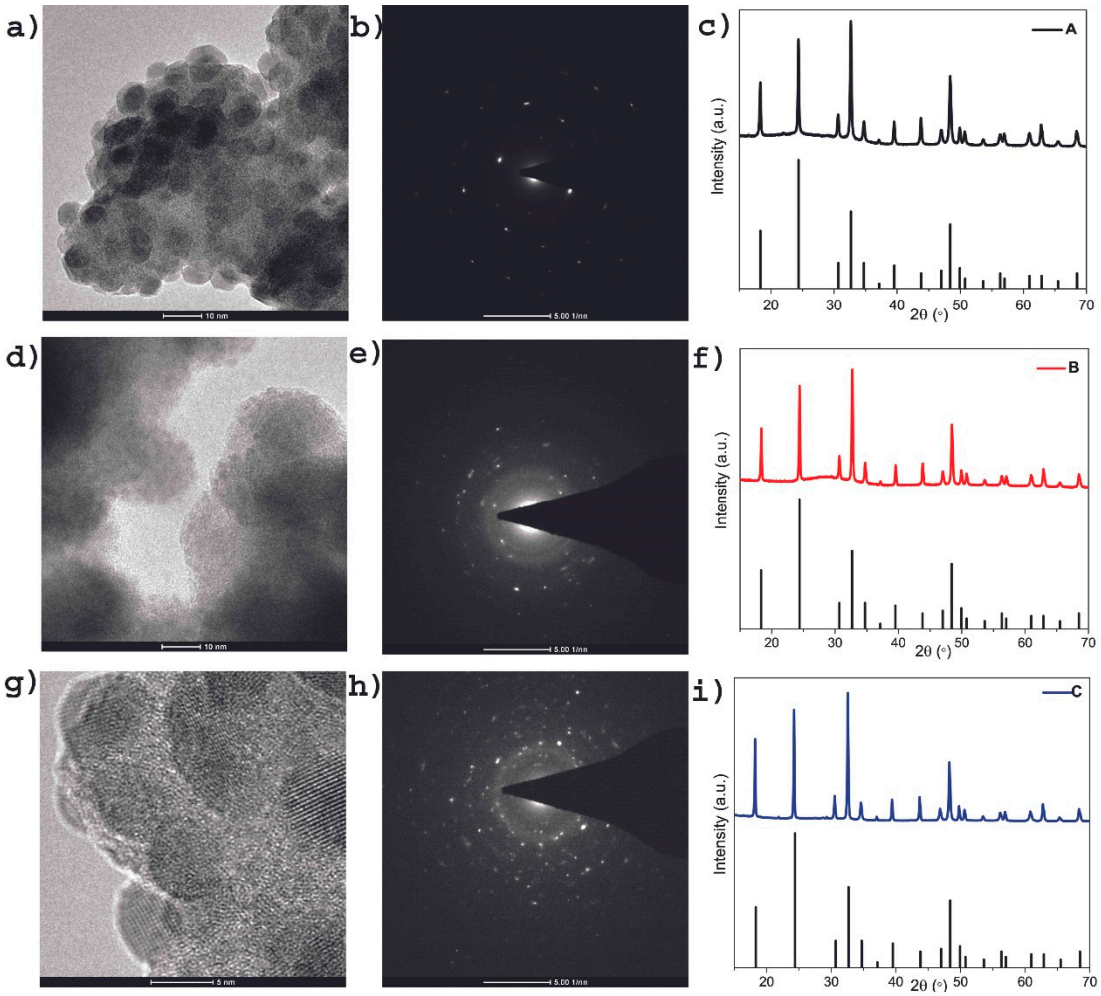

Figure 4. HRTEM images of colloidal tetragonal zircon-type nanostructured $BiVO_4$ samples: a) A, d) B and g) C. together with corresponding (b, e, h) XRD diffractograms obtained from FFT and (c, f, i) XRD patterns together with vertical bars from card reference (Card No. 00-014-0133) of tz-$BiVO_4$.

From these figures it could be concluded that the diameter of colloidal tetragonal zircon-type nanostructured $BiVO_4$ particles decreases as the concentration of precursor decreases. These findings from the HRTEM micrographs of the colloids A, B and C were fully supported by X-ray analysis of the powders A-tz, B-tz and C-tz obtained from the dispersions [70,71]. Moreover, the average crystallite sizes of 4–9.4 nm estimated from the XRD diffraction peaks by the Halder–Wagner method were consistent with the sizes evaluated from the TEM images. In particular, similar values of the crystalline domain size and microscopically estimated average particle size of the nanostructured $BiVO_4$ imply that each particle consists of a single crystallite. It is in accordance with theoretically estimated radii using Brus equation.

The obtained $BiVO_4$ particles crystallized in tetragonal zircon-type structure (space group I41/amd, a = b = 7.300 Å and c = 6.457 Å, JCPDS card no. 00-014-0133) and corresponding XRD patterns are given in Figure 4c, 4f and 4i. All patterns clearly show the presence of a single tetragonal zircon type phase of $BiVO_4$. The relatively intense reflection peaks suggest that the as-synthesized nanostructured $BiVO_4$ are highly crystalline. The effect of size-dependent lattice expansion in nanoparticles is observed. The size dependence can be explained naturally from the increasing surface-to-volume ratio and the sensitivity of the surface stress to environmental conditions. Also, point defects may cause lattice expansion in special cases, where the particles are not in thermodynamic equilibrium or where special effects modify the thermodynamic conditions [72].

 doi:10.20944/preprints202503.1940.v1

4. Conclusions

In summary, the colloidal dispersions of highly nanocrystalline tetragonal zircon-structured $BiVO_4$ particles with 2-8 nm in size were successfully prepared through a facile inexpensive room-temperature precipitation method using ethylene glycol simultaneously as a solvent, a reaction medium and a capping agent. The preparation procedure has proved to be fully reproducible over multiple runs and the as-prepared colloids have been stable and homogeneously colored over longer periods of time. The optical, structural and microstructural properties were examined in detail. The obtained band-gap values, using Tauc's plot, of 3.07, 3.09 and 3.12 eV are higher than the values for tz-$BiVO_4$ reported in literature before. X-ray photoelectron spectroscopy technique confirmed the occurrence of Bi, V, and O elements and also found that Bi and V exist in +3 and +5 oxidation states, respectively. The radius (r) of the nanoparticles was estimated theoretically using Brus equation. The findings from the HRTEM micrographs of colloidal dispersions were fully supported by X-ray analysis of the powders obtained from the dispersions. Similar values of the crystalline domain size and microscopically estimated average particle size of the nanostructured BiVO4 imply that each particle consists of a single crystallite. It is in accordance with theoretically estimated radii using Brus equation. Interesting experimental findings in photodegradation experiments with a suspension of tz-$BiVO_4$ catalyst powders and MO dye under simulated solar light were encouraging and deserve further, more elaborate investigation of poorly studied tz-$BiVO_4$. It was found that adsorption was the dominant mechanism by which the MO solution was purified, whereas photocatalysis played a minor role under indoor lighting conditions. The interactions between the p-electrons of the MO ring and the surface (-OH) groups dominated the mechanism according to which adsorption occurred. This study demonstrated that the ultrasmall $BiVO_4$ nanoparticles with tetragonal structure could be excellent candidate for wastewater treatment via their highly efficient adsorption and photocatalytic properties.

Author Contributions: Conceptualization, D.M. and M.F.; methodology, D.M.; software, G.C.R. and M.F.; validation, D.M. G.C.R., and M.F.; resources, D.M. and M.F.; writing—original draft preparation, D.M..; writing—review and editing, D.M. G:C:R. and M.F; funding acquisition, D.M. and M.F. All authors have read and agreed to the published version of the manuscript."

Funding: D.M. thanks to the Ministry of Science, Technological Development and Innovation of the Republic of Serbia (grant number 451-03-136/2025-03/ 200017).

Data Availability Statement: Data, Graphics and Figures that support the findings of this study are available from the corresponding author upon reasonable request.

Acknowledgments: The Authors thankful to Dr. Krisjanis Smits and Dr. Tanja Barudžija for providing TEM and XRD measurements.

Conflicts of Interest: The authors declare no conflicts of interest.

References

1. Liao, J.; Qi, T.; Chu, B.; Peng, J.; Luo, F.; Qian, Z. Multifunctional nanostructured materials for multimodal cancer imaging and therapy. *J. Nanosci. Nanotechnol.* **2014**, *14*, 175-189, https://doi.org/10.1166/jnn.2014.9049.
2. Chiappini, A.; Armellini, C.; Piccolo, V.; Zur, L.; Ristic, D.; Jovanovic, D.J.; Vaccari, A.; Zonta, D.; Righini, G.C.; Ferrari, M. Colloidal crystals based portable chromatic sensor for butanol isomers and water mixtures detection. *Opt. Mater.* **2019**, *90*, 152-158, https://doi.org/10.1016/j.optmat.2019.02.039.
3. Jovanović, D.J.; Chiappini, A.; Zur, L.; Gavrilović, T.V.; Tran, T.N.L.M; Chiasera, A.; Lukowiak, A.; Smits, K.; Dramićanin, M.D; Ferrari, M. Synthesis, structure and spectroscopic properties of luminescent $GdVO_4:Dy^{3+}$ and $DyVO_4$ particles. *Opt. Mater.* **2018**, *76*, 308-316, https://doi.org/10.1016/j.optmat.2017.12.046.
4. del Rosal, B.; Pérez-Delgado, A.; Carrasco, E.; Jovanović, D.J.; Dramićanin, M.D.; Dražić, G.; de la Fuente, Á.J.; Sanz-Rodriguez, F.; Jaque, D. Neodymium-based stoichiometric ultrasmall nanoparticles for

 doi:10.20944/preprints202503.1940.v1

multifunctional deep-tissue photothermal therapy. *Adv. Opt. Mater.* **2016**, *4*, 782-789, https://doi.org/10.1002/adom.201500726.

5. Periša, J., Antić, Ž.; Ma, C.-G.; Papan, J.; Jovanović, D.; Dramićanin, M,D, Pesticide-induced photoluminescence quenching of ultra-small Eu^{3+}-activated phosphate and vanadate nanoparticles. *J. Mater. Sci. Technol.* **2020**, *38*, 197-204, https://doi.org/10.1016/j.jmst.2019.09.004.
6. Ye, M.; Liu, X.; Iocozzia, J.; Liu, X.; Lin, Zhiqun, Chapter 1: Nanostructured materials for high efficiency perovskite solar cells. In *Nanomaterials for Sustainable Energy, Book NanoScience and Technology*, 1st Edition, Springer International Publishing, Cham, Switzerland, 2016, pp. 1-39, https://doi.org/10.1007/978-3-319-32023-6_1.
7. Cheng, B.; Lou, H.; Zeng, Z.; Liu, Y.; Zeng, Q.; Structural phase transition in $BiVO_4$ nanosheets under high pressure. *J. Phys. Chem. C* **2024**, *128*, 12267–12273, https://doi.org/10.1021/acs.jpcc.4c03113.
8. *Nanostructured and Advanced Materials for Fuel Cells*, 1st Edition, Jiang, S.P.; Shen, P.K. CRC Press, Taylor and Francis Group, Boca Raton, 2013, https://doi.org/10.1201/b16107.
9. Jafari, T.; Moharreri, E.; Amin, A.S.; Miao, R.; Song, W.; Suib, S.L. Photocatalytic water splitting-the untamed dream: A review of recent advances, *Molecules* **2016**, *21*, 900, https://doi.org/10.3390/molecules21070900.
10. Ghosh, S. Chapter 12: Promising inorganic nanomaterials for future generation. In *Applications of Multifunctional Nanomaterials, A volume in Micro and Nano Technologies*, Thomas, S.; Kalarikkal N.; Abraham, A.R. Elsevier Inc. 1000 AE Amsterdam, Netherlands, Oxford OX5 1GB, United Kingdom, Cambridge, MA 02139, United States, 2023, pp. 247-263. https://doi.org/10.1016/C2019-0-00946-6.
11. Cox, D.M. Chapter 4: High surface area materials. In *R&D Status and Trends in Nanoparticles, Nanostructured Materials and Nanodevices*, Siegel, R.W.; Hu, E.; Cox, D.M.; Goronkin, H.; Jelinski, L.: Koch, C.C.; Mendel, J.; Roco, M.C.; Shaw, D.T. Springer Dordrecht, 1999. https://doi.org/10.1007/978-94-015-9185-0.
12. Cao, X.; Gu, Y.; Tian, H.; Fang, Y.; Johnson, D.; Ren, Z.; Chen, C.; Huang, Y. Microemulsion synthesis of ms/tz-$BiVO_4$ composites: The effect of pH on crystal structure and photocatalytic performance. *Ceram. Int.* **2020**, *46*, 20788-20797, https://doi.org/10.1016/j.ceramint.2020.05.048.
13. Cheng, C.; Tan, H.; Zhu, W.; Liu, L.; Chen, K.; Yan, J. The transition of tetragonal to monoclinic phase in $BiVO_4$ coupled with peroxymonosulfate for photocatalytic degradation of tetracycline hydrochloride. *Environ. Res.* **2025**, *267*, 120631, https://doi.org/10.1016/j.envres.2024.120631.
14. Ribeiro, F.W.P.; Moraes, F.C.; Pereira, E.C.; Marken, F.; Mascaro, L.H. New application for the $BiVO_4$ photoanode: A photoelectroanalytical sensor for nitrite. *Electrochem. Commun.* **2015**, *61*, 1-4, https://doi.org/10.1016/j.elecom.2015.09.022.
15. David,W.I.F. Ferroelastic phase transition in $BiVO_4$: III. Thermodynamics. *J. Phys. C: Solid State Phys.* **1983**, *16*, 5093, https://doi.org/10.1088/0022-3719/16/26/006.
16. Qu, Z.; Liu,P.; Yang, X.;Wang, F.; Zhang, W.; Fei, C.Microstructure and characteristic of $BiVO_4$ prepared under different pH values: Photocatalytic efficiency and antibacterial activity. *Materials* **2016**, *9*, 129; https://doi.org/10.3390/ma9030129.
17. Obregón, S.; Colón, G. Heterostructured Er^{3+} doped $BiVO_4$ with exceptional photocatalytic performance by cooperative electronic and luminescence sensitization mechanism *Appl. Catal. B: Environ.* **2014**, *158–159*, 242–249, https://doi.org/10.1016/j.apcatb.2014.04.029.
18. Dragomir, M.; Arčon, I.; Gardonio, S.; Valant, M. Phase relations and optoelectronic characteristics in the $NdVO_4$-$BiVO_4$ system. *Acta Mater.* **2013**, *61*, 1126–1135, https://doi.org/10.1016/j.actamat.2012.10.020.
19. Polo, A.; Dozzi, M.V.; Marra, G,; Sivula, K.; Selli, E. Improving the photoelectrocatalytic efficiency of $CuWO_4$ through molybdenum for tungsten substitution and coupling with $BiVO_4$. *Sustain. Energy Fuels* **2024**, *8*, 3182-3191, https://doi.org/10.1039/d4se00161c.
20. Park, Y.; McDonald, K.J.; Choi, K.- S. Progress in bismuth vanadate photoanodes for use in solar water oxidation. *Chem. Soc. Rev.* **2013**, *42*, 2321-2337, https://doi.org/10.1039/C2CS35260E.
21. Xue, L.; Li-Li, Y.; Li-Na, Y.; Qing-Feng, G.; Yong-Sheng, Y.; Han, Z. Controllable synthesis and photocatalytic activity of spherical, flowerlike and threadlike bismuth vanadates. *Acta Phys. Chim. Sin.* **2013**, *29*, 1771-1777, https://doi.org/10.3866/PKU.WHXB201305131.

 doi:10.20944/preprints202503.1940.v1

22. Chen, Q.; Zhou, M.; Ma, Di.; Jing, D. Effect of preparation parameters on photoactivity of $BiVO_4$ by hydrothermal method. *J. Nanomater*. **2012**, *2012*, Article ID 621254, https://doi.org/10.1155/2012/621254.
23. Hunge, Y.M.; Uchida, A.; Tominaga,Y.; Fujii,Y.; Yadav, A.A.; Kang, S.-W.; Suzuki, N.; Shitanda, I.; Kondo, T.; Itagaki, M.; Yuasa, M.; Gosavi, S.; Fujishima, A.; Terashima, C. Visible light-assisted photocatalysis using spherical-shaped $BiVO_4$ photocatalyst. *Catalysts* **2021**, *11*, 460, https://doi.org/10.3390/catal11040460.
24. Zhang, X.; Liu,Y.; Zhai,Y.; Yu, Y.; Guo,Y.; Hao, S. An optimization strategy for photo-Fenton-like catalysts: Based on crystal plane engineering of $BiVO_4$ and electron transfer properties of 0D CQDs. *Environ. Res.* **2023**, *222*, 115347, https://doi.org/10.1016/j.envres.2023.115347.
25. Tan, G.; Zhang, L.; Ren, H.; Wei, S.; Huang, J.; Xia, A. Effects of pH on the hierarchical structures and photocatalytic performance of $BiVO_4$ powders prepared via the microwave hydrothermal method. *ACS Appl. Mater. Interfaces* **2013**, *5*, 5186-5193, https://doi.org/10.1021/am401019m.
26. Wang, X.; Liu, H.; Wang, J.; Chang, L.; Song, N.; Yan, Z.; Wan, X. Additive-free solvothermal preparation, characterization, and photocatalytic activity of 3D butterfly-like $BiVO_4$, *Res. Chem. Intermed.* **2015**, *41*, 2465-2477, https://doi.org/10.1007/s11164-013-1360-4.
27. Saison,T. Chemin, N.; Chanéac, C.; Durupthy, O.; Mariey, L.; Maugé, F.; Brezová, V.; Jolivet, J.-P. New insights into $BiVO_4$ properties as visible light photocatalyst. *J. Phys. Chem. C* **2015**, *119*, 12967−12977, https://doi.org/10.1021/acs.jpcc.5b01468.
28. Nagabhushana, G.P.; Tavakoli, A.H.; Navrotsky, A. Energetics of bismuth vanadate. *J. Solid State Chem.* **2015**, *225*, 187-192, https://doi.org/10.1016/j.jssc.2014.12.030
29. Nguyen, T.D.; Cao, V.D.; Nguyen, V.H.; Nong, L.X.; Luu, T.D.; Vo, D.-V.N.; Do S.T.; Lam, T.D. Synthesized $BiVO_4$ was by the co-precipitation method for Rhodamine B degradation under visible light. *IOP Conf. Ser.: Mater. Sci. Eng.* **2019**, *542* 012058, https://doi.org/10.1088/1757-899X/542/1/012058.
30. Bhattacharya, A.K.; Mallick, K.K.; Hartridge, A. Phase transition in $BiVO_4$, *Mater. Lett.* **1997**, *30*, 7-13, https://doi.org/10.1016/S0167-577X(96)00162-0.
31. Li, G.; Bai,Y.; Zhang, W.F.; Difference in valence band top of $BiVO_4$ with different crystal structure. *Mater. Chem. Phys.* **2012**, *136*, 930-934, https://doi.org/10.1016/j.matchemphys.2012.08.023.
32. Fan, H.; Jiang, T.; Li, H.; Wang, D.; Wang, L.; Zhai, J.; He, D.; Wang, P.; Xie, T. Effect of $BiVO_4$ crystalline phases on the photoinduced carriers behavior and photocatalytic activity. *J. Phys. Chem. C* **2012**, *116*, 2425–2430, https://doi.org/10.1021/jp206798d.
33. Fu, L.; Li, Z.; Shang, X. Recent surficial modification strategies on $BiVO_4$ based photoanodes for photoelectrochemical water splitting enhancement. *Int. J. Hydrogen Energy* **2024**, *55*, 611-624, https://doi.org/10.1016/j.ijhydene.2023.11.253.
34. Patial, B.; Bansal, A.; Gupta, R.; Mittal, S.K. $BiVO_4$-based heterojunction nanophotocatalysts for water splitting and organic pollutant degradation: a comprehensive review of photocatalytic innovation. *Rev. Inorg. Chem*. **2024**, *44*, 495-519, https://doi.org/10.1515/revic-2024-0009.
35. Zhao, Y.; Li, R.; Mu, L.; Li, C. Significance of crystal morphology controlling in semiconductor-based photocatalysis: A case study on $BiVO_4$ photocatalyst. *Cryst. Growth Des.* **2017**, *17*, 2923-2928, https://doi.org/10.1021/acs.cgd.7b00291.
36. Satyavir, T.; Praneetha, D.; Arumugam, S.; Murugan, V. Tetragonal to monoclinic crystalline phases change of $BiVO_4$ via microwave-hydrothermal reaction: in correlation with visible-light-driven photocatalytic performance. *Inorg. Chem.* **2019**, *58*, 5096–5110, https://doi.org/10.1021/acs.inorgchem.9b00193.
37. Zhang, H.M.; Liu, J.B.; Wang, H.; Zhang, W. X.; Yan, H. Rapid microwave-assisted synthesis of phase controlled $BiVO_4$ nanocrystals and research on photocatalytic properties under visible light irradiation. *J. Nanopart Res.* **2008**, *10*, 767-774, https://doi.org/10.1007/s11051-007-9310-y.
38. Dai, D.; Liang, X.; Zhang, B.; Wang, Y.; Wu, Q.; Bao, X.; Wang, Z.; Zheng, Z.; Cheng, H.; Dai, Y.; Huang, B.; Wang, P. Strain adjustment realizes the photocatalytic overall water splitting on tetragonal zircon $BiVO_4$. *Adv. Sci.* **2022**, *9*, 2105299, https://doi.org/10.1002/advs.202105299.
39. Wei, Z.; Zhu, Y.; Guo, W.; Liu, J.; Jiang, Z.; Shanggun, W. Enhanced photocatalytic overall water splitting via MOF-derived tetragonal $BiVO_4$-based solid solution. *J. Chem. Eng.* **2021**, *414*, 128911, https://doi.org/10.1016/j.cej.2021.128911.

40. Obregón, S.; Lee, S.W.; Colón, G. Exalted photocatalytic activity of tetragonal $BiVO_4$ by Er^{3+} doping through a luminescence cooperative mechanism. *Dalton Trans.* **2014**, *43*, 311-316, https://doi.org/10.1039/C3DT51923F.
41. Luo, Y.; Tan, G.; Dong, G.; Ren, H.; Xia, A. A comprehensive investigation of tetragonal Gd-doped $BiVO_4$ with enhanced photocatalytic performance under sun-light. *Appl. Surf. Sci.* **2016**, *364*,156-165, https://doi.org/10.1016/j.apsusc.2015.12.100.
42. Usai, S.; Obregón, S.; Becerro, A.I.; Colón, G. Monoclinic-tetragonal heterostructured $BiVO_4$ by yttrium doping with improved photocatalytic activity. *J. Phys. Chem. C* **2013**, *117*, 24479-24484, https://doi.org/10.1021/jp409170y.
43. Huang, J.; Tan, G.; Zhang, L.; Ren, H.; Xia, A.; Zhao, C. Enhanced photocatalytic activity of tetragonal $BiVO_4$: Influenced by rare earth ion Yb^{3+}. *Mater. Lett.* **2014**, *133*, 20-23, https://doi.org/10.1016/j.matlet.2014.06.123.
44. Gomes, L.E.; Nogueira, A.C.; da Silva, M.F.; Plaça, L.F.; Maia, L.J.Q.; Gonçalves, R.V.; Ullah, S.; Khan, S.; Wender, H. Enhanced photocatalytic activity of $BiVO_4$/Pt/PtOx photocatalyst: The role of Pt oxidation state. *Appl. Surf. Sci.* **2021**, 567, 150773, https://doi.org/10.1016/j.apsusc.2021.150773.
45. Saison, T.; Chemin, N.; Chanéac, C.; Durupthy, O.; Mariey, L.; Maugé, F.; Brezová, V.; Jolivet, J.-P. New insights into $BiVO_4$ properties as visible light photocatalyst, *J. Phys. Chem. C* **2015**, *119*, 12967-12977, https://doi.org/10.1021/acs.jpcc.5b01468.
46. Bhattacharya, A.K.; Mallick, K.K.; Hartridge, A. Phase transition in $BiVO_4$. *Mater. Lett.* **1997**, *30*, 7-13, https://doi.org/10.1016/S0167-577X(96)00162-0.
47. Glasser, F.P.; Woods, P. Preparation and properties of pigmentary grade $BiVO_4$ precipitated from aqueous solution. *Ceram. Int.* **2004,** *30*, 875-882, https://doi.org/10.1016/j.ceramint.2003.10.008.
48. Dolić, S.D.; Jovanović, D.J.; Smits, K.; Babić, B.; Marinović-Cincović, M.; Porobić, S.; Dramićanin, M.D. A comparative study of photocatalytically active nanocrystalline tetragonal zyrcon-type and monoclinic scheelite-type bismuth vanadate. *Ceram. Int.* **2018**, *44*, 17953-17961, https://doi.org/10.1016/j.ceramint.2018.06.272.
49. Dong, L.; Guo, S.; Zhu, S.; Xu, D.; Zhang, L.; Huo, M.; Yang, X. Sunlight responsive $BiVO_4$ photocatalyst: Effects of pH on L-cysteine-assisted hydrothermal treatment and enhanced degradation of ofloxacin. *Catal. Commun.* **2011**, *16*, 250-254, https://doi.org/10.1016/j.catcom.2011.05.005.
50. Tokunaga, S. Hideki Kato, Akihiko Kudo, Selective preparation of monoclinic and tetragonal $BiVO_4$ with scheelite structure and their photocatalytic properties. *Chem. Mater.* **2001**, *13*, 4624-4628, https://doi.org/10.1021/cm0103390.
51. Guisheng, L.; Dieqing, Z.; Jimmy, C.Y.; Ordered mesoporous $BiVO_4$ through nanocasting: A superior visible light-driven photocatalyst. *Chem. Mater*. **2008**, *20*, 3983-3992, https://doi.org/10.1021/cm800236z.
52. Sarkar, S.; Garain, S.; Mandal, D.; Chattopadhyay, K.K. Electro-active phase formation in PVDF–$BiVO_4$ flexible nanocomposite films for high energy density storage application. *RSC Adv.* **2014**, *4*, 48220-48227, https://doi.org/10.1039/C4RA08427F.
53. Alvarez, S. A cartography of the van der Waals territories. *Dalton Trans*. **2013,** *42***,** 8617-8636, https://doi.org/10.1039/C3DT50599E.
54. Lin, X.; Yu, L.; Yan, L.; Li, H.; Yan, Y.; Liu, C.; Zhai, H. Visible light photocatalytic activity of $BiVO_4$ particles with different morphologies. Solid State Sci. **2014**, *32*, 61-66, https://doi.org/10.1016/j.solidstatesciences.2014.03.018.
55. Zhao, H.; Wei, X.; Pei, Y.; Han, W. Enhancing photoelectrocatalytic efficiency of $BiVO_4$ photoanodes by crystal orientation control. *Nanomaterials* **2024**, *14*, 1870; https://doi.org/10.3390/nano14231870.
56. Park, Y.; McDonald, K.J.; Choi, K.-S. Progress in bismuth vanadate photoanodes for use in solar water oxidation. *Chem. Soc. Rev.* **2013**, *42*, 2321-2337, https://doi.org/10.1039/C2CS35260E.
57. Kudo, A.; Omori, K.; Kato, H. A novel aqueous process for preparation of crystal form-controlled and highly crystalline $BiVO_4$ powder from layered vanadates at room temperature and its photocatalytic and photophysical properties. *J. Am. Chem. Soc.* **1999**, *121*, 11459-11467, https://doi.org/10.1021/ja992541y.

58. Nikama, S.; Joshi, S. Irreversible phase transition in $BiVO_4$ nanostructures synthesized by a polyol method and enhancement in photo degradation of methylene blue. *RSC Adv*. **2016**, *6*, 107463-107474, https://doi.org/10.1039/C6RA14700C.
59. Brus, L.E. Electron-electron and electron-hole interactions in small semiconductor crystallites: The size dependence of the lowest excited electronic state. *J. Chem. Phys*. **1984**, *80*, 4403-4409, https://doi.org/10.1063/1.447218.
60. Liu, T.; Zhou, X.; Dupuisc, M.; Li, C. The nature of photogenerated charge separation among different crystal facets of $BiVO_4$ studied by density functional theory. *Phys. Chem. Chem. Phys.* **2015**, *17*, 23503-23510, https://doi.org/10.1039/C5CP04299B.
61. Cao, Z.; Song, X.; Chen, X.; Sha, X.; Tang, J.; Yang, Z.; Lv, Y.; Jiang, C. In situ photoelectrochemical-induced surface reconstruction of $BiVO_4$ photoanodes for solar fuel production. *RRL Solar* **2024**, *8*, 2400523, https://doi.org/10.1002/solr.202400523.
62. Gu, F.-f.; Chen, G.-h.; Kang, X.-l.; Li, X.; Zhou, C.-r.;Yuan, C.-l.; Yun, Y.; Yang, T. A new $BiVO_4/Li_{0.5}Sm_{0.5}WO_4$ ultra-low firing high-k microwave dielectric ceramic. *J. Mater. Sci*. **2015**, *50*, 1295-1299, https://doi.org/10.1007/s10853-014-8688-z.
63. Wang, G.; Ling, Y.; Lu, X.; Qian, F.; Tong, Y.; Zhang, J.Z.; Lordi, V.; Rocha Leao, C.; Li, Y. Computational and photoelectrochemical study of hydrogenated bismuth vanadate. *J. Phys. Chem*. *C* **2013**, *117*, 10957-10964, https://doi.org/10.1021/jp401972h.
64. Hunge, Y.M.; Uchida, A.; Tominaga, Y.; Fujii, Y.; Yadav, A.A.; Kang, S.-W.; Suzuki, N.; Shitanda, I.; Kondo, T.; Itagaki, M.; Yuasa, M.; Gosavi, S.; Fujishima, A.; Terashima, C. Visible light-assisted photocatalysis using spherical-shaped $BiVO_4$ photocatalyst. *Catalysts* **2021**, *11*, 460, https://doi.org/10.3390/catal11040460.
65. Liang, X.; Wang, P.; Tong, F.; Liu, X.; Wang, C.; Wang, M.; Zhang, Q.; Wang, Z.; Liu,Y.; Zheng, Z.; Dai, Y.; Huang, B. Bias-free solar water splitting by tetragonal zircon $BiVO_4$ nanocrystal photocathode and monoclinic scheelite $BiVO_4$ nanoporous photoanode. *Adv. Funct. Mater*. **2021**, *31*, 2008656, https://doi.org/10.1002/adfm.202008656.
66. Bulut, D.T. Exploring the dual role of $BiVO_4$ nanoparticles: unveiling enhanced antimicrobial efficacy and photocatalytic performance. *J. Sol-Gel Sci. Technol*. **2025**, *In Press*, https://doi.org/10.1007/s10971-025-06682-z.
67. Zhu, Z.; Zhang, L.; Li, J.; Du, J.; Zhang, Y.; Zhou, J. Synthesis and photocatalytic behavior of $BiVO_4$ with decahedral structure. *Ceram. Int*. **2013**, *39*, 7461-7465, https://doi.org/10.1016/j.ceramint.2013.02.093.
68. Aghakhaninejad, S.; Rahimi, R.; Zargari, S. Application of $BiVO_4$ nanocomposite for photodegradation of methyl orange. *Proceedings* **2019**, *9*, 52, https://doi.org/10.3390/ecsoc-22-05666.
69. Lei, B.-X.; Zhang, P.; Wang, S.-N.; Li, Y.; Huang, G.-L.; Sun, Z.-F. Additive-free hydrothermal synthesis of novel bismuth vanadium oxide dendritic structures as highly efficient visible-light photocatalysts. *Mater. Sci. Semicond. Process.* **2015**, *30*, 429–434. https://doi.org/10.1016/j.mssp.2014.10.044.
70. Lu, Y.; Shang, H.; Shi, F.; Chao, C.; Zhang, X.; Zhang, B. Preparation and efficient visible light-induced photocatalytic activity of m-$BiVO_4$ with different morphologies, *J. Phys. Chem. Sol.* **2015**, *85*, 44–50, https://doi.org/10.1016/j.jpcs.2015.04.016.
71. Ravidhas, C.; Josephine, A.J.; Sudhagar, P.; Devadoss, A.; Terashima, C.; Nakata, K.; Fujishima, A.; Raj, A.M.E.; Sanjeeviraja, C. Facile synthesis of nanostructured monoclinic bismuth vanadate by a co-precipitation method: Structural, optical and photocatalytic properties. *Mater. Sci. Semicond. Process.* **2015**, *30*, 343–351, http://dx.doi.org/10.1016/j.mssp.2014.10.026.
72. Diehm, P.M.; Goston, P.; Albe, K. Size-dependent lattice expansion in nanoparticles: reality or anomaly? *Chem. Phys. Chem.* **2012**, *13*, 2443 – 2454, http://dx.doi.org/10.1002/cphc.201200257.